Acta Materialia 216 (2021) 117088

Contents lists available at ScienceDirect

Acta Materialia

journal homepage: www.elsevier.com/locate/actamat

Full length article

Grain size dependent microstructure and texture evolution during dynamic deformation of nanocrystalline face-centered cubic materials

Heng Li[a,b], Tianju Chen[c], Weilin Li[b], Hualei Zhang[d], Shuang Han[a,*], Caizhi Zhou[e,*], Zibin Chen[b,*], Emmanuel A. Flores-Johnson[f,1], Luming Shen[f], Jianshe Lian[a], Irene J. Beyerlein[g,h], Xiaozhou Liao[b]

[a] Key Laboratory of Automobile Materials, Ministry of Education and College of Materials Science and Engineering, Jilin University, Changchun 130025, China
[b] Australian Centre for Microscopy & Microanalysis and School of Aerospace, Mechanical and Mechatronic Engineering, The University of Sydney, Sydney, NSW 2006, Australia
[c] Department of Materials Science and Engineering, Missouri University of Science and Technology, Rolla, MO 65409, USA
[d] State Key Laboratory for Mechanical Behavior of Materials, Xi'an Jiaotong University, Xi'an 710049, China
[e] Department of Mechanical Engineering, University of South Carolina, Columbia, SC 29208, USA
[f] School of Civil Engineering, The University of Sydney, Sydney, NSW 2006, Australia
[g] Department of Mechanical Engineering, University of California at Santa Barbara, Santa Barbara, CA 93106, USA
[h] Materials Department, University of California at Santa Barbara, Santa Barbara, CA 93106, USA

ARTICLE INFO

Article history:
Received 11 March 2021
Revised 5 June 2021
Accepted 10 June 2021
Available online 17 June 2021

Keywords:
Dynamic deformation
Nanocrystalline
Deformation mechanisms
Crystal plasticity
Texture

ABSTRACT

Evolution of microstructure and texture in nanocrystalline (nc) face-centered cubic materials subjected to high-strain-rate compression are investigated. Three nc materials, differing in grain size or stacking fault energy, namely, 27 nm Ni, 70 nm Ni, and a 27 nm NiCo alloy are deformed under high strain rates (8000–23000 s^{-1}) using the split-Hopkinson pressure bar technique. The transmission Kikuchi diffraction technique and discrete-crystal plasticity finite element (D-CPFE) simulations are used to evaluate structural evolution. Experimental results show that grain growth and grain refinement occurred in samples with small and large initial grain sizes, respectively, while all deformed materials evolve to a (110) texture. The D-CPFE simulations, built for grain-size dependent nc deformation with no fitting parameters, reveal that partial dislocation slip caused faster texture evolution than full dislocation slip. Comparison between experimental and simulation results suggests that the (110) texture is mainly generated by combined full and partial dislocation slip in the 27 nm and 70 nm Ni samples, and by partial dislocation slip alone in the NiCo alloy. Deformation twinning made almost no contributions to the observed texture evolution. Grain-boundary-mediated deformation facilitates grain coarsening, while partial dislocation activities help to promote dynamic stabilization and further refinement of the nano-grains. The highly coupled evolution of microstructure and texture during dynamic deformation is controlled by a synergy of grain size and strain rate effects.

1. Introduction

Structural metals can experience high-strain-rate impact when used in transportation vehicles, airplanes, spacecrafts, satellites and fusion reactors. Improving their strength and damage resistance for such extreme service conditions continues to be a microstructural design and manufacturing challenge [1–4]. In recent years, nanocrystalline (nc) metals, comprised of average grain sizes smaller than 100 nm, have consistently demonstrated outstanding strengths, with values reaching nearly one order of magnitude greater than those of their coarse-grained counterparts [5]. While the quasi-static mechanical responses of these ultra-strong materials have been extensively studied, their mechanical and structural behaviors at high strain rate (HSR) have not. The limited number of investigations on the dynamic behavior of nc materials, to date, have mainly focused on body-centered cubic metals, including Fe [6,7], W [8], Ta [9,10], and V [11]. These studies have found that

* Corresponding authors.
E-mail addresses: shuanghan@jlu.edu.cn (S. Han), caizhi@mailbox.sc.edu (C. Zhou), z.chen@sydney.edu.au (Z. Chen).
[1] Current address: CONACYT-Unidad de Materiales, Centro de Investigacion Cientifica de Yucatan, Merida, Yucatan, 97205, Mexico.

https://doi.org/10.1016/j.actamat.2021.117088
1359-6454/

the dynamic deformation of these nc metals is inhomogeneous in nature and shear banding is the dominant deformation mode.

A few recent observations have hinted at the potential of designing and manipulating advanced impact-tolerant nanostructured materials with face-centered cubic (FCC) crystal structures. Extremely high strength during shock loading was observed in nc Cu due to the suppression of grain boundary (GB) sliding under laser shock compression [12]. Ultra-high strength was also achieved in Ni-W alloys during high-speed nano-indentation [13]. These outstandingly high strengths were the result of pronounced positive strain-rate dependence of the flow stress of nc FCC metallic nanomaterials [14,15]. Discussions on the mechanisms that govern plasticity of nc FCC materials under HSR, however, remain controversial. It was reported that dislocation activity is a prevalent deformation mechanism, whereas deformation twinning is a difficult event in nc Ni under shock-loading conditions [16]. This outcome is in qualitative agreement with predictions from molecular dynamic (MD) simulations [17]. However, another study reported that nc Ni prefers twinning over deformation by extended partials, especially under HSR [18]. As another viewpoint, significant detwinning and noticeable grain growth facilitated by GB-mediated processes were reported in dynamically deformed nc NiFe alloy [19]. It is worth pointing out that most of these studies were limited to relatively small dynamic strains and the rapid changes in microstructure were not taken into consideration. In deformation conditions when the microstructure is not stable, changes in the primary deformation mechanism can be expected. Such microstructural evolution can also substantially affect mechanical response [20]. Therefore, a comprehensive analysis of microstructural evolution can provide more useful information to elucidate the high-strain-rate mechanical response of nc materials. Although the changes in microstructures of nc FCC metals and alloys during large-strain deformation have been systematically studied [21–23], the effects of strain rate and strain level on the underlying microstructural changes have not.

Polycrystalline materials, including nc materials, tend to have or develop non-random orientation distributions or texture. Analysis of texture evolution during deformation can often provide fruitful information about the underlying deformation mechanisms, particularly in the case of nc materials [24–26]. For example, substantial texture development occurred in Ni with grain sizes ranging from 3 to 500 nm under high external pressures [27,28], indicating that dislocation activity can occur even within grains of nanometer dimensions. The texture evolution of a Ni-60% Co alloy [29] indicated deformation twinning and shear banding during cold rolling, while in a Ni-40% Co alloy [30] texture evolution was found to be mainly controlled by dislocation slip and shear banding. In [21], the combined effects of stacking fault energy (SFE) and grain size on the microstructure and texture evolution in a series of NiCo alloys during cold rolling were systematically investigated. The experimental and crystal plasticity simulation results suggested a transition in deformation mechanism from GB-mediated processes to full dislocation slip in low-Co containing alloys and partial-dislocation-controlled deformation in high-Co containing alloys. Systematic X-ray diffraction studies of the microstructure and texture evolution in an nc Pd–10 at. % Au alloy treated by high-pressure torsion [23] also implied a transition in deformation mechanisms, but from dislocation-slip-dominated to a GB-sliding-dominated deformation. These results demonstrate that texture analysis, especially when combined with microstructure analysis, is a powerful method for revealing the active and dominate mechanisms of nano-plasticity. No analogous experimental study, to date, has focused on texture evolution in nc metals and alloys under high-strain-rate deformation. This is in part due to the difficulty in simultaneously acquiring quantitative information on microstructure and grain orientation at the nano-scale. The relatively low spatial resolution of conventional Electron backscatter diffraction (EBSD) technique hinders it from analyzing nanostructured materials [31].

In the present study, the evolution of microstructure and texture of two nc FCC materials, pure Ni and NiCo alloy, subject to high-strain-rate dynamic deformation was investigated using the transmission Kikuchi diffraction (TKD) technique and discrete-crystal plasticity finite element (D-CPFE) simulations. The advantage of TKD over conventional EBSD lies in its significant improvement in spatial resolution, shown to range from 2–10 nm for wide variety of materials, while at the same time, maintaining the ability for rapid measurement of phase and crystallographic orientations and giving useful information such as grain size distribution, grain misorientation, GB character and crystallographic texture [32]. It provides an ideal tool for detecting both texture and nanoscale features [33]. Over the years, the conventional, rate-dependent elasto-visco-plastic CPFE constitutive model, has been extensively used to study texture evolution in nanostructured materials (including nc Ni [34], nc Cu [35], and two-phase nanolayered materials [36,37]) under various deformation conditions. However, they explicitly accounted for nanograin size effects by adding grain size and adjustable parameters in the hardening law. Doing so allowed these models to capture the grain size effect on strength and texture evolution in agreement with several experimental studies of nc Cu and Ni. In this work, we employ a different model D-CPFE to study the grain-size dependent stress–strain responses of nc Ni and NiCo alloy. The advantage of the D-CPFE model is that it does not rely on fitting parameters.

As we will show, the combined experimental and computational analysis of the evolution in microstructure and texture during dynamic compression of nc Ni and NiCo suggest the activation of and transition between different deformation mechanisms, including grain rotation, GB sliding and migration, dislocation slip, and deformation twinning. The findings provide insight into the effects of grain size and strain rate on the mechanical response under shock loading.

2. Experimental methods

2.1. Materials and processing

Two batches of bulk nc Ni sheets were synthesized via direct-current electrodeposition from an electrolyte containing nickel sulfate, nickel chloride, boric acid and some surfactants (saccharin and 1, 4-butynediol, which acted as stress relievers and grain-refining agents). To adjust the grain size, the current density was varied, and different amounts of surfactants were added to the bath. A Ni-37% Co alloy (mass percent, hereinafter referred to as the NiCo alloy) sheet was deposited via direct-current electrodeposition from the same bath but with certain amounts of cobalt sulfate added. The bath temperature was kept at 60 °C. Bright-finished stainless-steel sheets (100 × 100 × 3 mm^3) and high purity Ni sheets (99.9%) were used as the cathode and anode, respectively. After depositing for 24 h in order to reach a thickness of about 1 mm, the samples were mechanically stripped from the stainless-steel substrates for testing. The chemical homogeneity of the as-deposited NiCo samples was examined using energy dispersive X-ray spectroscopy (EDS) in transmission electron microscopy (TEM). The results revealed uniform chemical distributions from both the plan view (Fig. S1) and the cross section (Fig. S2) within the resolution limit of the EDS detection. The main impurities in the three deposited films are sulfur and carbon, both of which are from the surfactants (Table S1). The mean grain size of the pristine nc NiCo alloy is ~27 nm (hereafter refer to as the 27 nm NiCo). The initial grain size of the two batches of nc Ni are ~27 nm and ~70 nm,

respectively. Hereinafter they are referred to as the 27 nm Ni and 70 nm Ni material.

Cylindrical samples with a diameter of ~3 mm were cut from the deposited sheets by electrical discharge machining and then polished to attain a flat and smooth surface using sandpapers with grades of 600, 2000, and 5000. The final thickness of these disc samples was 600–650 μm. High-strain-rate uniaxial compression experiments were performed at room temperature using the split Hopkinson pressure bar (SHPB) technique at different combinations of strain (up to 0.56) and strain rate (up to 26,000 s^{-1}). The dynamic compression strain was estimated by the reduction in the specimen thickness ($\varepsilon = (\eta_0 - \eta)/\eta_0$), where η_0 and η are the initial and final thickness of the sample, respectively.

2.2. Characterization methods

As-deposited materials and deformed materials were cut into discs with a diameter of 3 mm and mechanically ground to a thickness of ~80 μm using 1200 and 4000 grid sandpapers. A Struers TenuPol-5 twin-jet electropolisher was used to etch a hole at the center of the discs, by applying constant electrolyte flow jetting on both sides of the discs. For this step, the electrolyte solution contained 25% nitric acid and 75% methanol. The operating voltage and temperature were 8 V and −14 °C, respectively. Precision ion milling system (PIPS) was used to clean the surface of the specimens and broaden the hole and was applied for about 5 minutes, operating at 0.3 KV with dual beams tilted at ±3°. After this step, the specimens were used for both the TKD and TEM analyses. Specimens for plan-view and cross-sectional EDS examinations are prepared using tripod polishing. They were grounded using diamond lapping films with diamond grain sizes of 30, 9, 3, and 1 μm, followed by ion milling using a Gatan model 691 PIPS with beam voltage of 4 kV and milling angle of ±5°.

Bright-field (BF) TEM images and high-resolution TEM (HRTEM) images were captured using a JEOL JEM 2200FS TEM operating at 200 kV. BF TEM imaging and Scanning TEM (STEM)-EDS mapping and line-scan were carried out using a Thermo Fisher Scientific Themis-Z double-corrected microscope equipped with ChemiSTEM (Super-X) X-ray detectors operating at 300 kV. Characterization of grain size, grain orientation and the fraction of twin and GB were carried out by the TKD technique, using a Zeiss ULTRA plus field emission gun scanning electron microscope, equipped with an Oxford Instrument Channel 5 EBSD system and a Nordlys-S EBSD detector. All TKD scans were taken in the sample normal direction. The operations thereafter consisted of placing the specimens on a 20° pre-tilted holder, operating the EBSD mode under 30 kV with high current, elevating the work distance to 6.5 mm, and finally, inserting the EBSD detector to around 6 mm. The step size used for data collection was 4 nm and the scanning area was 1.4 × 1.4 μm^2. TKD data analysis was conducted using the commercial Channel 5 software (Tango and Membo). The density of geometrically necessary dislocations (GNDs) was calculated using in-house codes, which are based on the Kernel Average Misorientation (KAM) method with a square kernel, taking only the pixels on the periphery of the kernel into account. KAM measurements are a popular method to measure the local misorientation, and KAM values can be obtained directly from TKD map data. KAM values were calculated by averaging crystal orientation differences between the host pixel and adjacent neighboring pixels. In this study, a filter size binning of 5 × 5 pixel and a sub-grain angle of 5° were employed [38]. The change of the fraction of Σ3 {111} twin boundaries was monitored to illustrate the variation of twin boundaries. Twin boundaries were defined by a misorientation of 60° with a tolerance of 8.66°, according to Brandon's criterion [39], regardless of their coherent/incoherent character.

3. D-CPFE simulations

3.1. The D-CPFE model

In present work, the D-CPFE model developed in [40] for nanocrystals is extended to account for plastic deformation via the motion of both partial and full dislocations and then applied to calculate the texture evolution in nc Ni and NiCo during deformation. The original model takes into account the effect of size of the nanograins on dislocation nucleation via its limitation on the length of discrete dislocation sources from GBs and on the extent of dislocations can glide across the grain [40]. In prior work, the ability of the model to capture grain size effects on strength was demonstrated for single phase metals [40,41], nano-twinned metals [42] and two-phase nanolayered metals [43]. Below, we provide a brief review of the model formulation before presenting the extension to partial dislocation plasticity.

In the D-CPFE model, a conventional, rate-dependent elasto-viscoplastic constitutive model is employed, which accounts for elastic and plastic deformation of crystals. The underlying kinematic relations developed by Marin et al. [44] are modified here to accommodate the discrete CPFE model formulation. According to crystal plasticity theory, the plastic velocity gradient $\mathbf{L}^p$ is given by:

$$\mathbf{L}^p = \sum_{\alpha=1}^{N} \dot{\gamma}^\alpha \boldsymbol{s}^\alpha \otimes \boldsymbol{m}^\alpha \tag{1}$$

where N is total number of slip systems in the crystal, $\dot{\gamma}^\alpha$ is the shear strain rate of slip system α, $\boldsymbol{s}^\alpha$ and $\boldsymbol{m}^\alpha$ are the slip direction and slip plane normal of slip system α, respectively, and the product $\boldsymbol{s}^\alpha \otimes \boldsymbol{m}^\alpha$ defines the Schmid tensor.

The corresponding shear strain rate in slip system α is calculated with a power-law flow rule, given by

$$\dot{\gamma}^\alpha = \dot{\gamma}_0 \left[\frac{|\tau^\alpha|}{\tau^\alpha_{CRSS}} \right]^{\frac{1}{m}} sign(\tau^\alpha) \tag{2}$$

where $\dot{\gamma}_0$ is a reference shear strain rate, τ^α and τ^α_{CRSS} are the resolved shear stress (RSS) and critical resolved shear stress (CRSS) in slip system α, respectively, and m is the strain rate sensitivity exponent.

In the D-CPFE formulation, the plastic strain within each nanograin is assumed to be carried by moving dislocations originating solely from sources in the GBs. The stress to activate these GB sources, τ^α_{CRSS}, is controlled by the length L of the GB source. It is assumed that the stress to propagate the dislocation segment L from the GB onto the glide plane τ^α_{CRSS} is also sufficient to sustain its glide across the entire grain cross section. After glide across the grain, the dislocation is presumed to be fully absorbed by the GB on the other side of the glide plane in the same grain. The threshold emission stress, τ^α_{CRSS}, can be related to L via Foreman's formula [45]:

$$\tau^\alpha_{CRSS} = \frac{\mu b}{2\pi L} \log\left(\frac{L}{r_0}\right) \tag{3}$$

where μ is the effective shear modulus, b is the magnitude of the Burgers vector, L is dislocation source length, and r_0 is dislocation core size, which is set as $2b$. The calculated τ^α_{CRSS} from Eq. (3) is used in Eq. (2) to generate the shear strain rate in each slip system.

Due to fluctuations in local stress state and defect structure, dislocation emission from the GB triple junction varies spatially and temporally [46]. The upper and lower limits of L are the dislocation core size and the grain size D, respectively. The direct consequence of the statistically varying L for a given D is a grain-size dependent CRSS distribution, wherein for random variable L, there is a unique τ^α_{CRSS} determined from Foreman's formula, Eq. (3). It has

Table 1
List of parameters used in the D-CPFE model.

Samples	Ni	Ni-37Co
Shear modulus (GPa)	76.0	74.11
Magnitude of Burgers vectors for partial dislocations (nm)*	0.1443	0.1442
Total strain (%)	54	86.5
C_{11} (GPa)	246.5	238.7
C_{12} (GPa)	147.3	155.3
C_{44} (GPa)	124.7	131.5

*The magnitude of Burgers vectors for partial dislocations was calculated by $|b| = a_o/\sqrt{6}$, where a_o is the lattice constant.

been shown [40,41] that for a uniformly varying L the τ^{α}_{CRSS} distribution follows the generalized extreme value distribution. Because D is the upper limit on L, D affects both the mean value and the dispersion in the τ^{α}_{CRSS} distribution. Larger D leads to lower mean and standard deviation in τ^{α}_{CRSS}.

In terms of the temporal variation of dislocation nucleation, dislocation sources nucleated consecutively at the same GB triple junction can differ in length, leading to varying τ^{α}_{CRSS} for each individual dislocation emission. To model this feature, once a new slip event is activated, a new τ^{α}_{CRSS} value is randomly sampled from the τ^{α}_{CRSS} distribution for a given grain size and assigned to the slip system. When a dislocation glides across a nanograin, a discrete shear strain is generated:

$$\gamma_{discrete} = \frac{b}{D} \tag{4}$$

Thus, in the discrete CPFE model, a grain size effect is introduced in many ways [40,41]: D affects the minimum value, mean value, and dispersion in τ^{α}_{CRSS} distribution and $\gamma_{discrete}$ is inversely proportional to D.

3.2. Extension to glide by partial dislocations

To model the deformation and texture evolution of the nc Ni and NiCo, partial dislocation slip is considered in this study, which was neglected in prior versions of the D-CPFE model [40]. Each grain has 12 FCC $\frac{1}{6}\langle 112\rangle\{11\bar{1}\}$ slip systems available for deformation. The CRSS for partial dislocation slip is made up of the line tension evaluated by Eq. (3) and the back stress induced by the stacking fault (SF) generated by partial dislocations, i.e., $\tau^{partial}_{CRSS} = \tau_{line\ tention} + \tau_{back\ stress}$. Based on a density functional theory-phase field dislocation dynamics calculation [47], the back stress, $\tau_{back\ stress}$, is around 3.6 GPa in Ni. Since there is no data for the back stress in Ni-37Co, we set the back stress for Ni-37Co also equal to 3.6 GPa. The other parameters used in the D-CPFE calculations are listed in Table 1.

The D-CPFE method already considers the strain rate effect on dislocation activities. The dependence lies in the flow rule, which contains a reference shear strain rate, $\dot{\gamma}_0$. As commonly done in standard CPFE calculations, this rate is set equal to the experimental strain rate [40–43]. Since the material was tested at the same temperature, the calculations did not take into account temperature-dependent flow stress. According to the work in Ref. [27], texture formation during the deformation of nanocrystalline materials still mainly arises from dislocation glide within the nano-sized grains, even within grains smaller than 10 nm. Thus, the contribution of GB sliding to texture evolution was considered sufficiently smallto be neglected in the present treatment.

3.3. Model set-up

The simulation model consists of 10 × 10 × 10 grains as shown in Fig. 1, which is of the optimum balance between computation precision and time. Each grain is modeled by a C3D8R brick element with reduced integration (i.e., one integration point). Displacement controlled uniaxial compression is imposed along the Z- direction and periodic boundary conditions (PBC) are imposed on all directions.

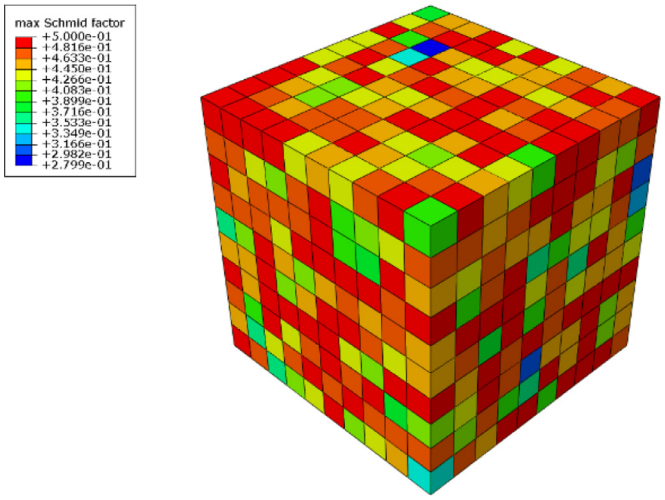

Fig. 1. Schematic of the CPFE model consisting of 10 × 10 × 10 elements. Each element represents a single grain and is colored according to its maximum Schmid factor.

The constitutive model, written as a user-defined material (UMAT) subroutine, is implemented into ABAQUS finite element software. The material parameters needed are the elastic moduli and Burgers vectors of the partial and full dislocations. The flow rule in Eq. (2) introduces a rate sensitivity parameter m, for which we use 0.1, a common value for FCC materials, and reference strain rate, for which we set to be the applied rate. There are no adjustable parameters used in any of the calculations here for the nc Ni and NiCo alloy.

The initial textures used in calculations are built based upon the experimental textures. One thousand grains were randomly picked from the experimental dataset and their corresponding orientations were assigned in the model nc microstructure. Fig. 2 compares the initial experimental and model textures of pure Ni and NiCo, confirming the consistency between the experiment and simulation.

4. *Ab initio* calculations

Ab *initio* calculations were performed using the exact muffin-tin orbitals (EMTO) method [48] with the coherent-potential approximation (CPA) [49]. The self-consistent and total energy calculations were performed by adopting the Perdew-Burke-Ernzerhof (PBE) [50] exchange-correlation functional. The CPA [49] was adopted to treat the chemical disorders in NiCo solid solution. The generalized planar fault energy (GPFE) curves were calculated by adopting

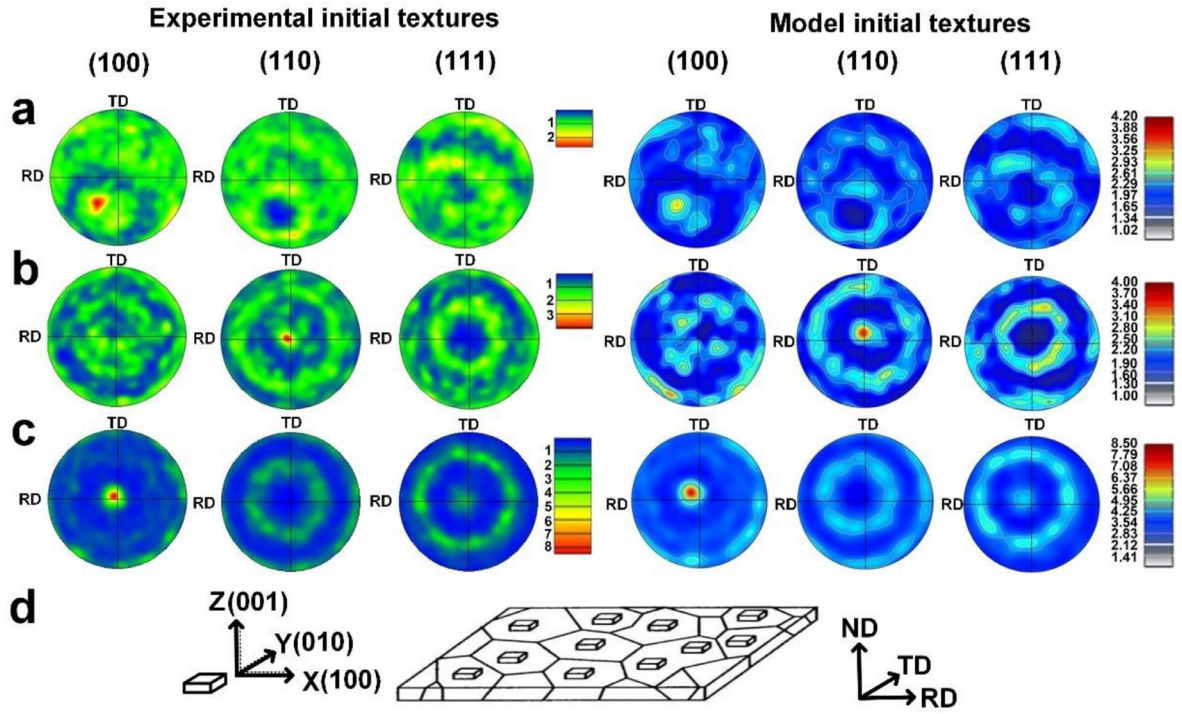

Fig. 2. Textures of undeformed samples of (a) nc Ni with d = 27 nm; (b) nc Ni with d = 70 nm; (c) nc NiCo with d = 27 nm. (Pole figures on left and right columns are from experimental and model textures, respectively.) (d) Schematic sketch showing the three principal directions defined in the material coordinate system: normal direction (ND), rolling direction (RD) and transverse direction (TD), which are applied to all the IPF maps and pole figures throughout the paper.

a 12-layer supercell with and without one fault per unit cell [51]. The GPFE was calculated as $\gamma_{GSFE} = (E^{\text{fault}} - E^0)/A$, where E^{fault} and E^0 are the total energies of supercell with and without the fault, respectively, A is the stacking fault area. We calculated the total energy E at the measured lattice constant.

5. Results

5.1. Texture evolution

From the pole figures in Fig. 3, texture evolution can be clearly identified in the 27 nm NiCo alloy during dynamic deformation. Before dynamic deformation, a strong (100) texture was detected in the as-deposited sample, yet with deformation, it was eliminated and a noticeable (110)-type texture evolved in its place, after reaching a strain of 0.43. With more strain, this texture further intensified. Despite beginning with more random initial texture, deformation-induced texture evolution of the 27 nm Ni sample proceeded in the same way as that in the nc NiCo alloy. The (110) texture appears after dynamic compression (Fig. 4a,b). The intensity of the (110) texture in 27 nm nc Ni (Fig. 4b) is weaker than that in 27 nm NiCo alloy (Fig. 3d) compressed to similar strain levels of 0.54 and 0.56. The as-deposited 70 nm Ni clearly displays a (110) texture (Fig. 4c), unlike the random texture observed in the as-deposited 27 nm Ni. The difference in initial texture might be due to the varying deposition conditions [52] and different amounts of surfactants used in the baths [53]. In the nc Ni sample, both the (110)-type texture and its intensity remained almost unchanged during dynamic compression (Fig. 4d).

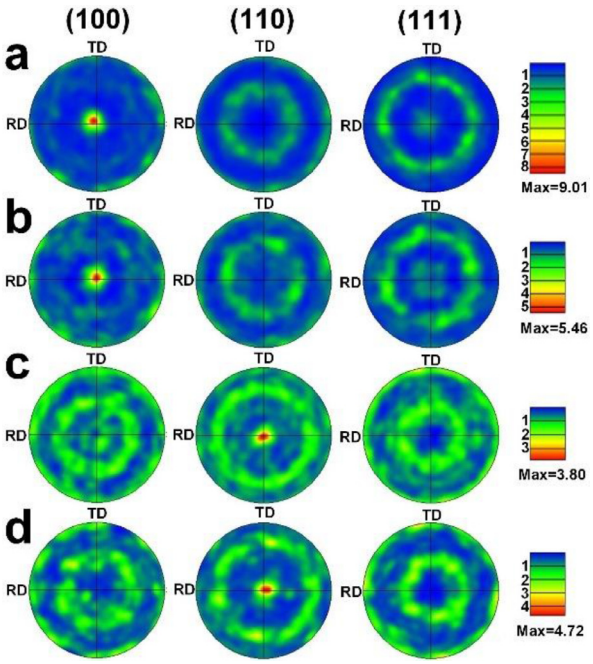

Fig. 3. Pole figures for 27 nm NiCo alloy samples with dynamic strains of (a) 0, (b) 0.21, (c) 0.43 and (d) 0.56.

5.2. Textures predicted by the D-CPFE model

Figs. 5 and 6 show the textures predicted by the D-CPFE model for 27 nm NiCo, 27 nm Ni and 70 nm Ni, respectively. In Fig. 5, the predicted textures of 27 nm NiCo alloy from the partial dislocation model agree well with the experimental ones both qualitatively and quantitatively. The deformed texture evolved to a (110)-type texture from the initial (100)-type texture. Although the initial textures for 27 nm nc Ni and 70 nm nc Ni are different, both full- and partial-dislocation models predicted a strong (110) type texture in these two samples (Fig. 6), consistent with the experimental results shown in Fig. 4. It is worth pointing out that, ac-

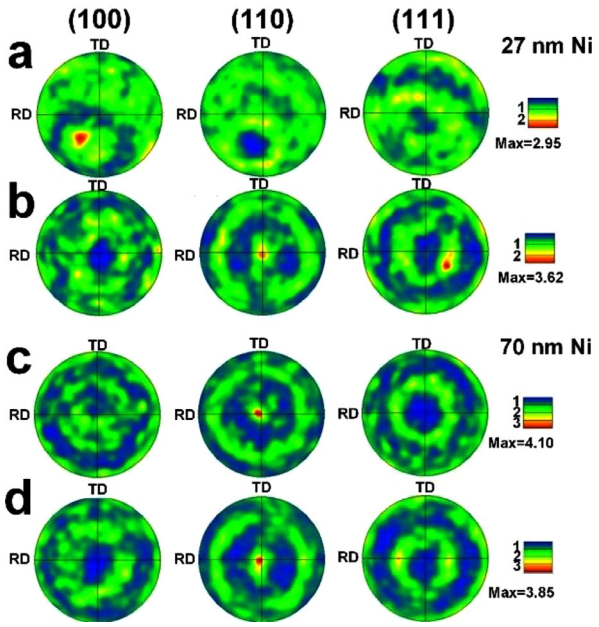

Fig. 4. Pole figures for (a) as-deposited 27 nm Ni sample, (b) 27 nm Ni sample with dynamic strain of 0.54, (c) as-deposited 70 nm Ni sample and (d) 70 nm Ni sample with dynamic strain of 0.56.

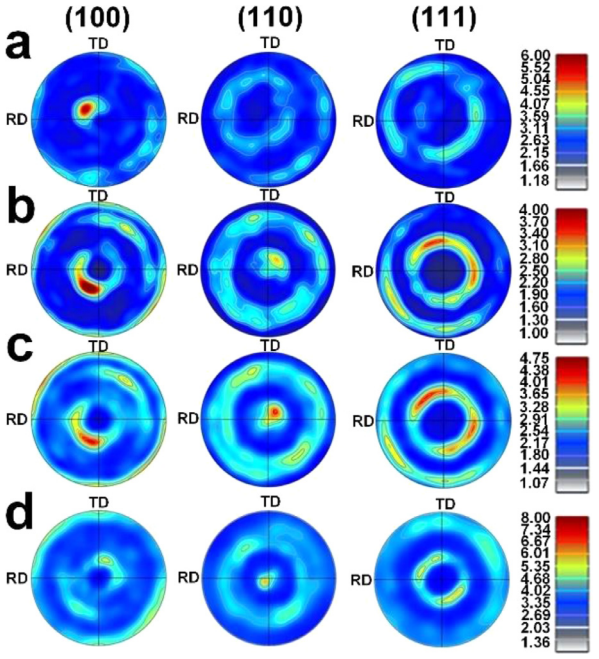

Fig. 5. Calculated textures of deformed nc NiCo of 27 nm by the model allowing for partial dislocation glide at strains of (a) 0, (b) 0.21, (c) 0.43 and (d) 0.56.

cording to the present simulation results, partial dislocation slip leads to faster texture evolution compared to full dislocation slip. Altogether, the calculated deformed textures agree with the experimental textures, which is notable since the model does not use any adjustable parameters or directly imposes a grain size effect. Discrepancies in texture intensities may result from the fact that any GB sliding or migration or activity from both full and partial slip were not taken into account in the D-CPFE model.

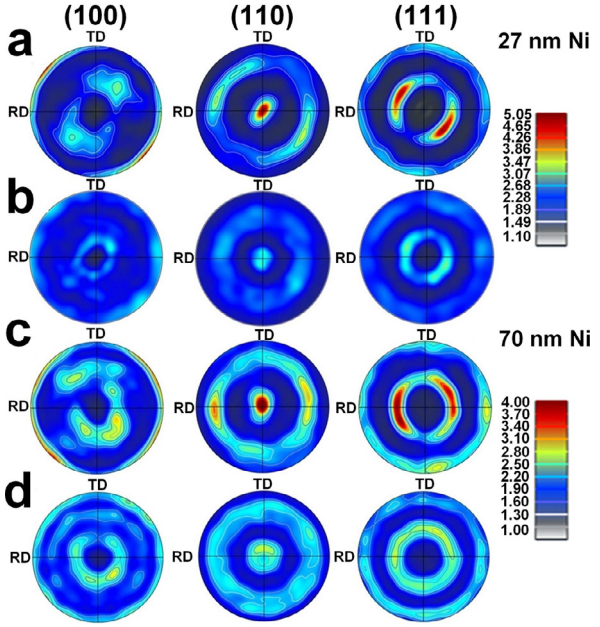

Fig. 6. Calculated textures of deformed 27 nm Ni to a strain of 0.54 by the model (a) only allowing for partial dislocation glide and (b) only considering full dislocation glide. Calculated textures of deformed 70 nm Ni to a strain of 0.56 by the model allowing for (c) only partial dislocation glide and (d) only considering full dislocation glide.

5.3. Microstructure evolution

Typical microstructures of the as-deposited and dynamically compressed nc NiCo and Ni samples are shown in Figs. 7 to 12. Plan-view inverse pole figure (IPF) maps and the corresponding statistic grain size distribution charts of the as-deposited samples indicate that the initial structures of all the three materials consisted of equiaxed grains (Figs. 7a, 10a and 11a). Some columnar grains can be observed in the cross-section view of 27 nm NiCo alloy and Ni (Fig. S3 a, b), but the column lengths are much smaller than sample thickness. In 70 nm Ni, the columnar grains are not so apparent, which might be due to a relatively larger grain size and wider size distribution (Fig. S3 c).

Upon high-strain-rate deformation, both the mean grain size and grain size distribution of the 27 nm NiCo alloy compressed at strain of 0.21 (Fig. 7b) remain nearly the same as those in the as-deposited sample. Increasing the compressive strain to 0.43 led to continuous grain growth. In the most-deformed sample with a strain of 0.56, the average grain size grew to 52 nm, which is more than twice the initial value (Fig. 7c,d), and the grain size distribution broadened. Detailed TKD misorientation map of a sample compressed to the strain of 0.43 reveal some relatively large grains (d = ~100 nm) consisting of subgrains with small-angle sub-grain boundaries (sub-GBs). As an example, Fig. 8a shows four such large grains composed of subgrains marked with “I” to “IV”. The sub-GBs can be more clearly seen in the boundary maps shown in Fig. 8b, where they are marked by green dashed lines according to the distribution of low-angle grain boundaries (LAGB, 2~10°, marked by blue lines) in Fig. 8a. The shape and size of these subgrains are comparable with those in the as-deposited sample. This indicates that the large grains are likely the result of the coalescence of smaller ones.

The occurrence of grain rotation and coalescence is also supported by the change of other microstructural features. Fig. 9a shows the distribution of GBs in the as-deposited sample and samples compressed to different levels of strain. The LAGBs and high-angle grain boundaries (HAGBs, >10°) are presented by blue and

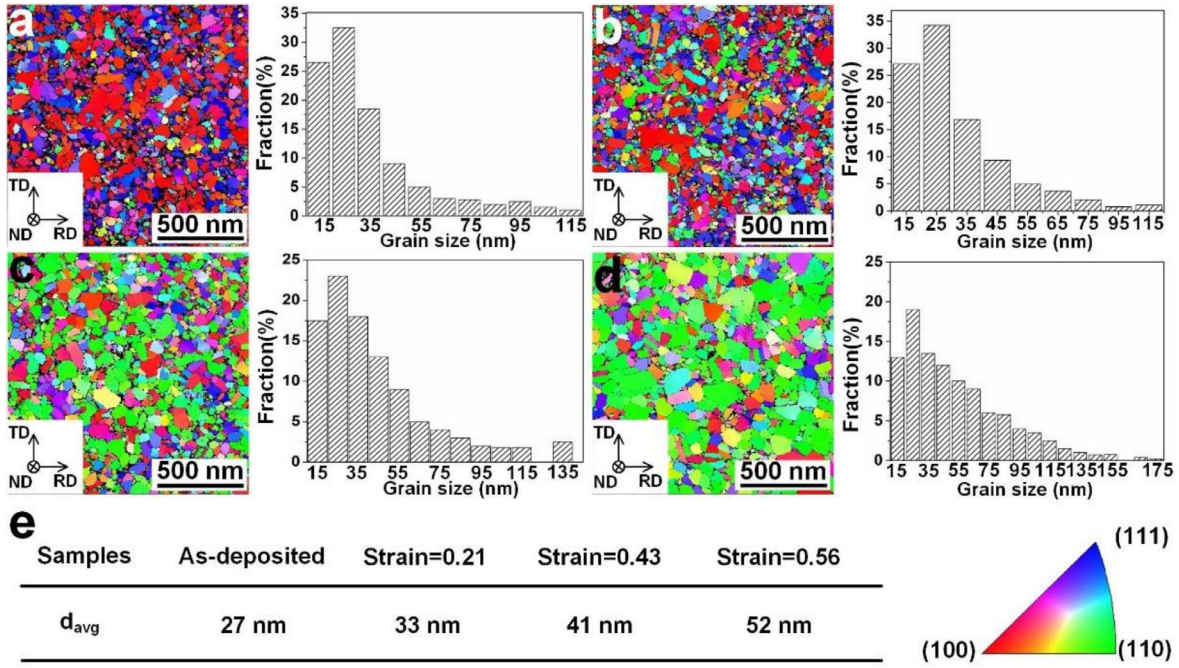

Fig. 7. IPF maps from TKD scans and the corresponding grain size distributions of (a) the as-deposited NiCo sample and (b–d) NiCo samples compressed to the strains of (b) 0.21, (c) 0.43 and (d) 0.56. The table in (e) gives the detailed values of mean grain sizes at different strains.

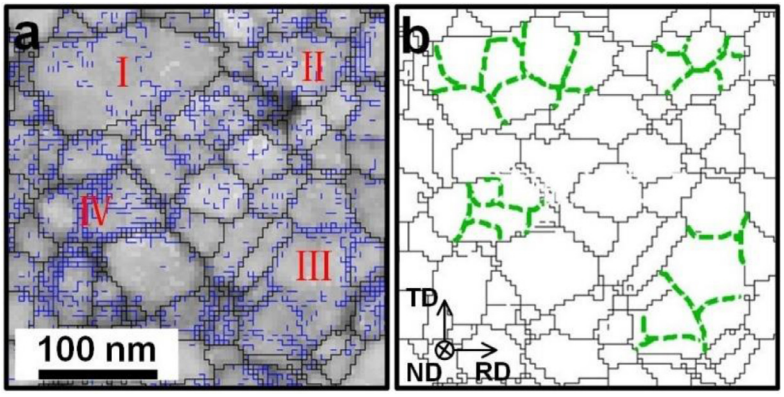

Fig. 8. (a) Representative misorientation map of four large grains in the deformed NiCo sample. Numbers I to IV represent four different large grains, each containing a distribution of LAGBs (blue dashed lines). (b) Corresponding boundary map clearly showing sub-GBs marked by green dashed lines. (For interpretation of the references to color in this figure legend, the reader is referred to the web version of this article.)

black lines, respectively. Fig. 9b presents the distribution of GNDs of these samples. These TKD results reveal that increasing strain (1) decreases the fraction of LAGBs from 36.7% to 21.9% and (2) reduces the density of GNDs from ~7.8 × 10^{15} m^{-2} in the as-deposited sample to 4.8 × 10^{15} m^{-2} in the sample deformed to a strain of 0.56. It is generally accepted that plastic deformation in nc materials is inhomogeneous [54] and that such plastic inhomogeneity would be exacerbated under HSR [55,56]. As a result, GNDs formed at GBs to maintain the strain compatibility between various grains [57]. Merging of small grains into larger ones eliminates the LAGBs from which accumulated GNDs are forced to become gliding dislocations, decreasing the number of LAGBs and the density of GNDs. From the growth twins in the as-deposited sample., the fraction of twin boundaries (TBs) experienced a slight reduction from 20.7 to 16.3% upon dynamic loading, as shown in the TB distribution maps in Fig. 9c.

Dynamic deformation (strain of 0.54) also induced observable grain growth in 27 nm Ni to a mean grain size of ~48 nm and broadened the grain size distribution (Fig. 10b). Among the other structural features, the fraction of LAGBs in the deformed sample remained ~5%, about the same as in the as-deposited material (Fig. 10c,f). The density of GNDs (Fig. 10d,g) decreases with accumulated strain from 1.1 × 10^{16} to 8.7 × 10^{15} m^{-2}, whereas the fraction of TBs (Fig. 10e,h) increases from 16.2 to 20.9% over the same strain range.

The 70 nm Ni shows a completely different microstructure evolution from the 27 nm Ni and NiCo alloy. The mean grain size of the compressed 70 nm Ni sample (strain of 0.56) reduced to 56 nm and the grain size distribution narrowed (Fig. 11b). Accordingly, with accumulated strain, the fraction of LAGBs decreased from 10% to 8.5% (Fig. 11c,f) while the density of GNDs increased from 4.6 × 10^{15} to 7.7 × 10^{15}/m^2 (Fig. 11d,g). The as-deposited 70 nm nc Ni was composed of grains with a broad grain size distribution ranging from 20 to 320 nm. During dynamic deformation, the elimination of large grains (100–320 nm), significant reduction in the number of medium grains (50–100 nm), and a boost in the number of very small grains (10–30 nm) were observed. These microstructural changes suggest fragmentation of large nano-grains

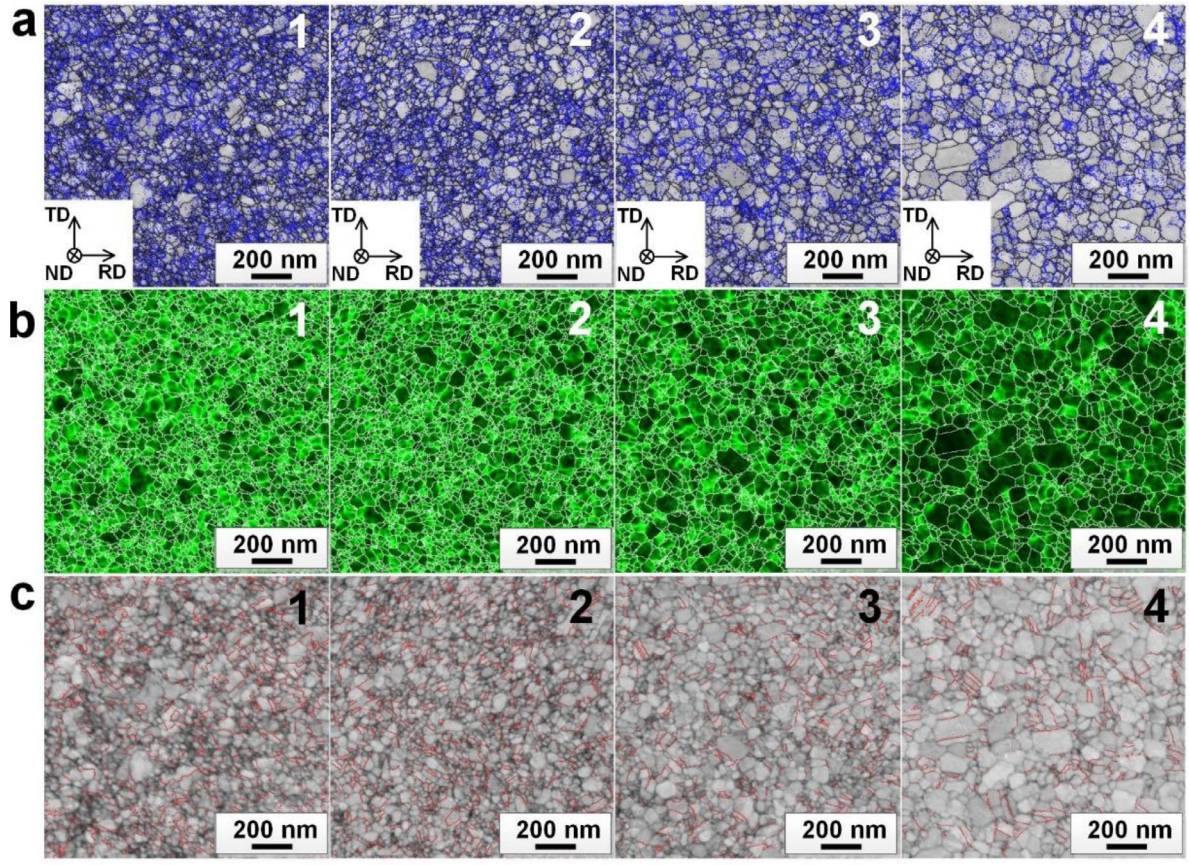

d

	As-deposited	Strain=0.21	Strain=0.43	Strain=0.56
LAGB	36.7%	30.2%	29.9%	21.9%
GND(* 10^{14})	78	73	63	48
TB	20.7%	18.7%	15.3%	16.3%

Fig. 9. (a) GB distribution maps, (b) GND distribution maps and (c) TB distribution maps of nc NiCo alloy upon high-strain-rate compression. The numbers 1 to 4 correspond to dynamic strains of 0, 0.21, 0.43 and 0.56, respectively. Blue and black lines in (a) represent LAGBs and HAGBs, respectively. The green part in (b) represents a high intensity of GNDs. The red-line in (c) represent TB. The table in (d) presents the values of LAGB, GND and TBs at different strains. (For interpretation of the references to color in this figure legend, the reader is referred to the web version of this article.)

into small ones and that the minimum refined grain size attainable during dynamic deformation is approximately 10–30 nm. Such values are much smaller than the grain size attainable during severe plastic deformation-induced grain refinement (100–140 nm in Ni) via dislocation-based mechanisms [58].

Microstructural analyses on these dynamically deformed materials hint at the activation of other refining mechanisms beyond the conventional dislocation-based ones. First, the fraction of TBs increased from 12 to 16% (Fig. 11e,h) with accumulated strain and nano-twins appeared in the deformed nano-grains with high frequency (Figs. 11h and 12). These nano-twins developed profusely over the entire grain, dividing the original grain into smaller parts. Some TBs even became curved as a result of the accumulation of high dislocation densities around them, as marked by the red arrows in Fig. 12. These curved TBs gradually became incoherent and eventually transform into HAGBs [59]. Although Ni exhibits a high energy barrier for deformation twinning (DT), the HSR introduced by shock loading made it possible to produce many twins in the nc Ni, as discussed in Section 6.1.3. In addition, some extremely small grains appeared to organize into a mosaic pattern within a relatively large “parent” grain (Fig. 12, blue arrows). Portions of the GBs of these small grains coincided with the GBs of the parent grain. It is very likely that these grains formed through a GB split and migration process: The original GB split off into separated segments and then the stress-assisted migration of the cleaved segments form a new grain. Although this GB splitting/migration mechanism was predicted previously by MD simulations [60], it has never been experimentally identified. The important distinction of the present observation is that previous investigations deformed at quasi-static strain rates that were several orders of magnitude lower than those in MD simulations. The HSR and shear stress generated during our SHPB tests make the activation of such mechanism possible. Taken together, we believe that the extremely small achievable grain size was largely facilitated by the HSR.

5.4. Dynamic mechanical behavior

Fig. 13 displays representative true stress–strain curves of the nc Ni and NiCo alloy dynamically compressed under strain rates of 19,000 to 23,000 s^{-1}. The dynamic plastic deformation of these three materials can be divided into three distinct stages. The stress peak, regime I, is followed by precipitous stress collapse, regime II, and then finally steady plastic flow, regime III. Since the SHPB was not able to capture the elastic part accurately, the stress peak in

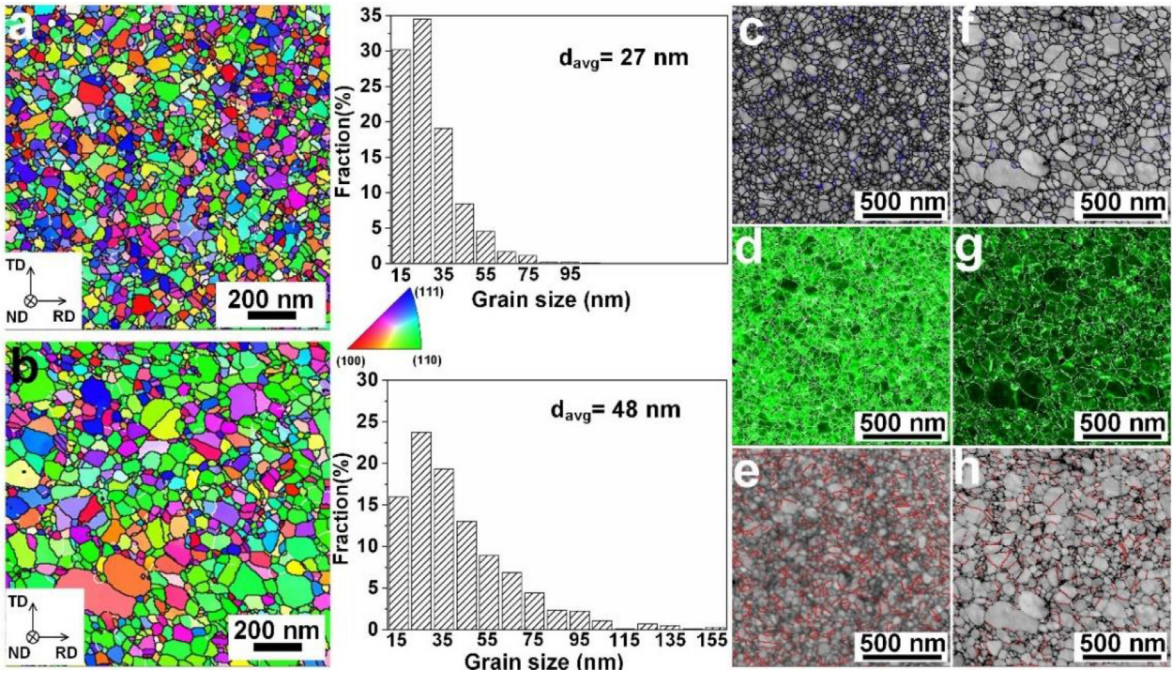

Fig. 10. IPF maps and grain size distribution histograms of the 27 nm Ni. (a) as-deposited sample. (b) sample dynamically compressed to a strain of 0.56. (c), (d) and (e) give the GB distribution map, GND distribution map and TB distribution map in the as-deposited sample, respectively. Corresponding maps of the dynamically compressed sample are shown in (f–h).

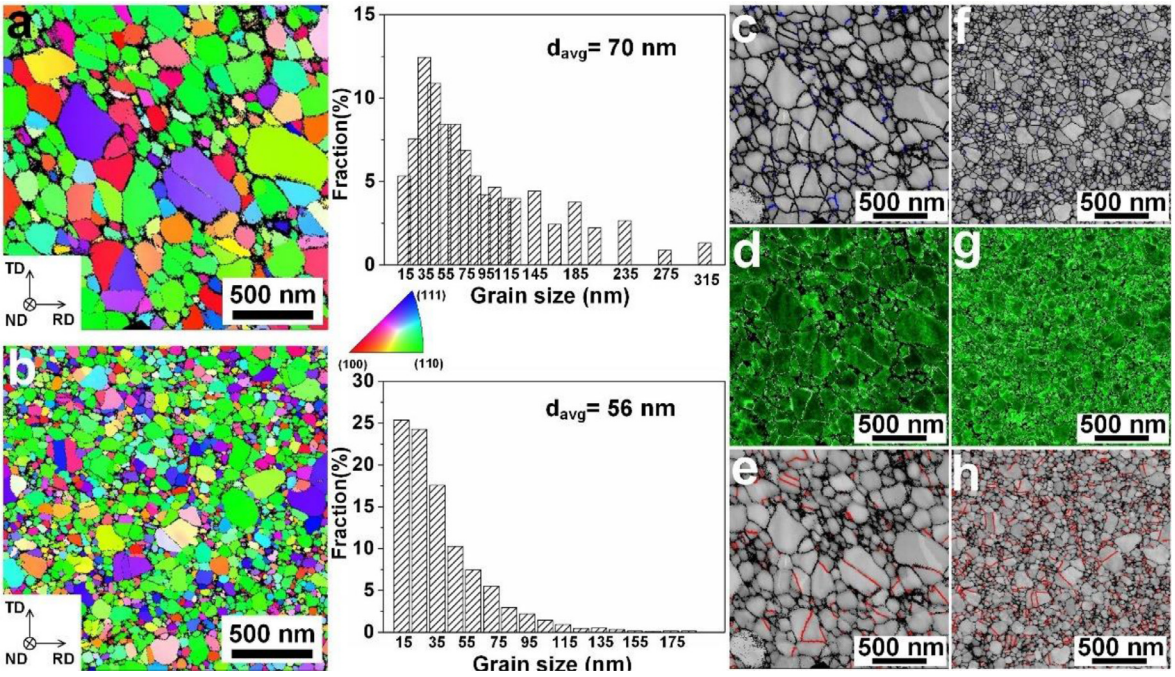

Fig. 11. IPF maps and grain size distribution histograms of the 70 nm Ni. (a) As-deposited sample. (b) Sample dynamically compressed to a strain of 0.56. (c), (d) and (e) give the GB distribution map, GND distribution map and TB distribution map in the as-deposited sample, respectively. Corresponding maps of the dynamically compressed sample are shown in (f–h).

regime I is used to determine the starting point of the dynamic plastic flow [61]. The stress collapse in regime II is a common occurrence during dynamic compression of nanostructured metals and alloys due to softening caused by adiabatic temperature rise [10,61]. Careful examination of the plastic flow behavior in regime III reveals distinctive differences for the three nc materials. The stress–strain curves of both 27 nm Ni and NiCo alloy exhibit flow softening. In sharp contrast, the 70 nm Ni shows near-perfect plastic behavior. Particularly, a nonnegligible strain hardening can be observed in 70 nm Ni at large strains (>0.4). The oscillations observed in the high-strain-rate curves are a consequence of the experimental technique, and thus, do not represent materials response. All three nc materials exhibit large dynamic compression plasticity and no sample failure was detected during tests. The strain obtained from the true stress–strain curve is higher than the values based on thickness measurement. This difference might be

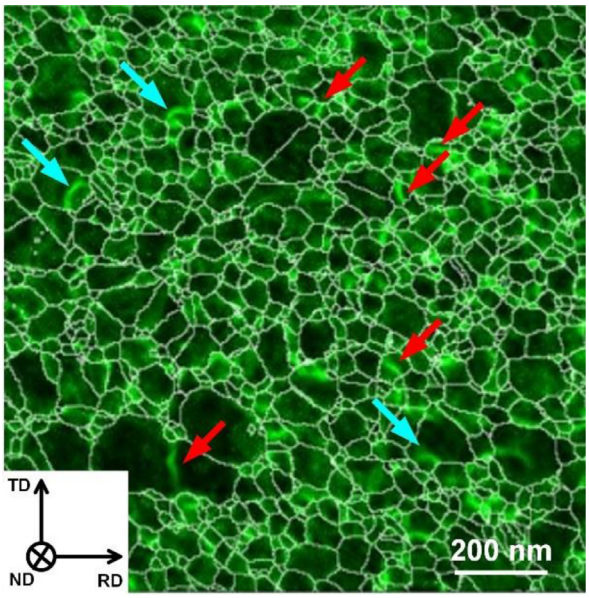

Fig. 12. Representative GND distribution map of deformed 70 nm nc Ni sample. TBs and split GBs that bow-out into nano-grains are highlighted by red and blue arrows, respectively. Accumulations of GNDs around the TBs and split GBs can be clearly seen. (For interpretation of the references to color in this figure legend, the reader is referred to the web version of this article.)

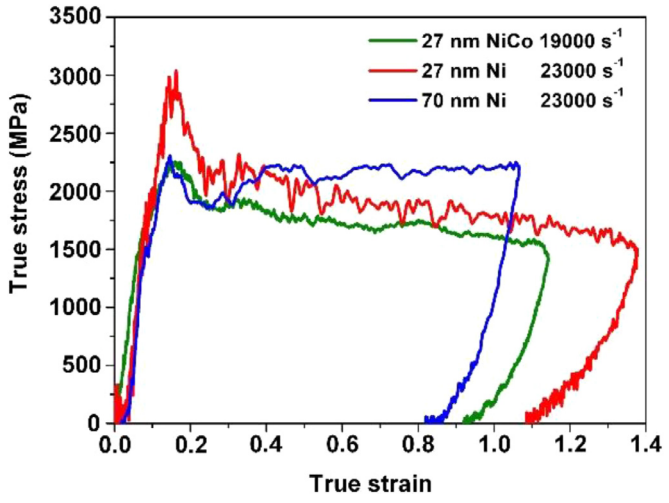

Fig. 13. Representative dynamic true stress-strain curves of nc Ni and NiCo alloy with strain rates ranging from 19000 to 23000 s^{-1}.

caused by the heat-induced lattice expansion under dynamic loading, which can be recovered when the sample cooled down after unloading.

6. Discussion

The foregoing results involving TKD data and D-CPFE simulations reveal three remarkable features during dynamic deformation: (i) Regardless of the initial texture, a (110)-type texture developed during dynamic deformation in all three nc materials (ii) Significant grain-size dependent microstructure evolution, i.e., grain coarsening was seen in the 27 nm NiCo and Ni, while the nano-grains in the 70 nm Ni underwent further refinement, which is seldom reported in nc metals; (iii) Different microstructure evolution routes induced distinct dynamic mechanical responses in these three nc materials. In what follows, we discuss the role of grain size, SFE and strain rate played on the evolutions of microstructure and texture.

6.1. Influences of grain size and strain-rate on texture evolution

6.1.1. Role of GB-mediated processes

For the 27 nm NiCo alloy, one elementary observation from both TKD experiments and simulations is the gradual weakening of the initial (100) texture at the early stages of dynamic deformation (with strain around ~ 0.21). Plastic deformation involving dislocation activities generally leads to lattice reorientation, and hence evolution of crystallographic texture [62]. The present texture model, involving discrete dislocation glide, simulates accurately the disappearance of pre-existing (100) texture in the nc NiCo alloy and concomitant increase in the intensities of the (111) and (110) textures with deformation (Fig. 5). However, experimental observations revealed that the initial (100) texture gradually faded, while no new texture can be detected below the strain of 0.21. The discrepancy between the experimental observation and the model calculation suggests that other mechanisms, beyond dislocation slip, are responsible for the texture evolution. The non-crystallographic mechanisms, such as GB-mediated deformation processes, including GB sliding, GB migration and grain rotations, can also weaken the pre-existing texture without introducing any new textures. So, it is highly possible that the weakening of the initial (100) texture at relatively low strain levels was attributed to the operation of GB-mediated deformation processes.

6.1.2. Role of dislocation slip

In the 27 nm Ni and the NiCo alloy, the (110) texture, a typical texture of FCC polycrystalline metals with intensive dislocation slip [63], gradually emerged with accumulated strain. This outcome signifies a shift from GB-mediated to dislocation-dominated dynamic deformation due to continuous grain coarsening. Previous experimental and computational studies have indicated that the dislocation mechanisms in nc materials are strongly grain-size dependent: When the grain size becomes smaller than a critical level, dislocations emitted from GBs would be partial dislocations in lieu of full dislocations [64]. In the partial-dislocation-dominant regime, emission of a leading partial from GB would leave a SF behind. If this leading partial is followed by a trailing partial on the same slip plane, an extended full dislocation is formed, and if another partial is emitted on the adjacent slip plane, a nano-twin is formed. The D-CPFE model also considers the different types of dislocation activities in nc materials. Our partial slip model considers the back stress induced by generated SFs, the value of which was calculated based on the phase-field model [37]. It represents a highly localized state of stress generated in a nc material and is likely much higher than that which would be expected in a coarse-grained material. We show that the number of slip events per grain in partial slip is larger than that in full slip in Fig. S4. More slip events with partial slip results from the smaller value Burgers vectors of the Shockley partial dislocations. Consequently, partial slip results in faster texture evolution. To the best of our knowledge, this is the first crystal plasticity based model that can predict not only the trend but also the rate of texture evolution under dynamic loading, which makes it possible to predict dislocation activities by evaluating the texture intensity.

Careful examination of texture evolution reveals that the 27 nm Ni exhibits lower (110) texture evolution rate than the 27 nm NiCo alloy during dynamic deformation. This hints that the dislocation activities prevailed in 27 nm NiCo alloy and 27 nm Ni might be different. According to the *ab initio* calculated GPFE curve of NiCo alloy (Fig. S5), the stable SFE of NiCo alloy is very low. Moreover, the ratio between stable SFE (γ_{sf}) and unstable SFE (γ_{usf})

Table 2
Calculated critical shear stress for full and partial dislocations in nc Ni.

Grain size (nm)	τ_f (MPa)	τ_p (MPa)
27	836	1447
48	528	1298
56	466	1268
70	388	1230

for NiCo alloy is only 0.1, which means the energy increase necessary for nucleating a trailing partial is extremely high [18]. Thus, partial dislocation slip is expected to play a key role in the development of the (110) texture in the 27 nm NiCo alloy within the strain range tested, which is further asserted by the observed texture evolution. The simulated textures assuming partial dislocation slip agreed better quantitatively with the experimental ones than those assuming full dislocation slip. For nc Ni, the simulation results revealed that when only full dislocation slip is considered, the simulated texture intensity is much lower than the experimental results, whereas the simulation model involving only partial dislocation slip yielded a texture that is much stronger than those found experimentally. The discrepancy between the experiments and simulations suggests that both full and partial dislocations are likely active carriers of dynamic deformation in the two sets of nc Ni, contributing simultaneously to the formation of (110) texture. This explains why 27 nm Ni and 27 nm NiCo alloy exhibit distinct (110) texture evolution rates. In the former both full and partial dislocation accommodate plastic deformation but in the later only partial dislocation prevails. According to the analytical model by Zhu et. al. [65], for nc materials the critical stress for moving a full (τ_f) and a partial dislocation (τ_p) is given by

$$\tau_f = \frac{Ga}{2\sqrt{2}\pi(1-\nu)d\cos\alpha} ln\frac{\sqrt{2}d}{a} \tag{5}$$

$$\tau_p = \frac{1}{\cos(\alpha+30^\circ)}\left[\frac{\sqrt{6}\lambda}{a} + \frac{Ga(4-\nu)}{8\sqrt{6}\pi(1-\nu)d}\right] ln\frac{\sqrt{2}d}{a} \tag{6}$$

where ν is the Poisson's ratio, λ is the stable SFE, a is the lattice parameter, d is the grain size and G is the shear modulus. The calculated τ_f and τ_p for nc Ni with various grain sizes are shown in Table 2. The maximum flow stress achieved in the two sets of nc Ni was ~2000 MPa during dynamic deformation. This can be transformed to a maximum shear flow stress of ~1000 MPa on the slip plane inclined 45° to the shock direction. Comparison of these stress values reveals that a combination of full and partial slip is plausible as increases in strain rate can increase local stress to overcome the high-energy barrier for many kinds of dislocation mechanisms [17,66]. Another factor that should be taken into consideration is the dynamically induced variation in the grain size. Growth in the sizes of the grains in the 27 nm Ni may have facilitated a transition from partial slip to full slip, while an inverse transition can be reasonably anticipated in 70 nm Ni due to grain fragmentation.

6.1.3. Role of deformation twinning

HSR is known to promote DT in metallic materials [66]. In FCC metals and alloys, DT usually induces a strong (100) fiber texture [67]. However, it is clearly demonstrated here that during dynamic deformation, the initial (100) component of nc NiCo alloys gradually diminishes. The TKD analysis indicates a decrease in twin density (Fig. 9c,d). TEM observations also reveal a relatively small number of grains containing twins even in the most-deformed sample (Fig. S6). For nc Ni, although TKD results reveal slightly increased twin densities during dynamic deformation, again, no (100) type texture can be detected in the deformed samples. These results indicate that although DT might be an accommodation deformation mechanism, its contribution to the texture evolution, whether in nc Ni or NiCo alloy, is limited. In nc materials, DT is substantially influenced by the GPFE and the so called twinning tendency, T, depends on the ratio between unstable SFE (γ_{usf}) and unstable twin fault energy (γ_{utf}). According to one proposed by Asaro and Suresh [68], T is given by

$$T = \sqrt{\left[1 + 2\left(1 - \frac{\gamma_{sf}}{\gamma_{usf}}\right)\frac{\gamma_{sf}}{\gamma_{usf}}\right]} \tag{7}$$

with $T > 1$ favoring DT. The T value for NiCo alloy is as high as 1.61, revealing ultra-high twinning tendency [69]. T is 1.33 for Ni from our present DFT calculations, which is comparable with previously reported values and means that Ni also exhibits a moderate tendency to twin [17,18]. So, the observed scarcity of DT is anomalous and is somewhat different from some previous studies suggesting DT as a preferred deformation mode in nc materials under high strain rate [18,70]. It is worth noting that most of these previous studies were limited to relatively small dynamic strains and the rapid change of microstructure during dynamic deformation was not taken into consideration. The abnormal twinning behavior we observed here can be rationalized based on grain size effects on DT in the nc regime, which is significantly influenced by the dynamic changes in grain size under shock loading.

It was reported that GPFE alone cannot predict accurately the twinnability of nc metals and alloys [64]. It is the GPFE and grain size working together to determine whether or not twinning occurs. In nc materials, a twin nucleates when twinning partials glide across the grain on the adjacent slip planes after the leading partial generates a SF across a grain [64], and there exists an optimum grain size for twinning [70]. In the optimum grain size regime, the critical stress for twin nucleation is lowest but outside of this regime, the stress required to emit a twinning partial becomes higher than the applied stress, which stops twinning but still allows the emission of the leading partials to create extended SFs [71]. The optimum grain size can be determined by [65,72]:

$$\frac{d_m}{ln\left(\sqrt{2}d_m/a\right)} = \frac{9.69-\nu}{253.66(1-\nu)}\frac{Ga^2}{\lambda} \tag{8}$$

and the minimum critical stress for DT within the optimum grain size range can be calculated as:

$$\tau_m = \frac{(5.69-2.02\nu)\lambda}{2a} \tag{9}$$

The d_m values for Ni and NiCo were calculated to be 23 nm and 36 nm, respectively. HSR tends to shift d_m to larger values. For instance, for nc Ni, d_m was reported to be ~50 nm under a strain rate of 2.6×10^3 s^{-1} by SHPB tests [70]. Thus, it is reasonable that d_m of the nc NiCo alloy under dynamic deformation will be larger than 50 nm. Careful examination of the grain size distributions in nc NiCo alloy (Fig. 7) illustrates that during the entire dynamic deformation, only a small number of grains, say, around 10%, falls within the optimum grain size range for twinning. So, it is conjectured that DT is not a preferred dynamic deformation mode in the present nc NiCo alloy. It is also worth pointing out that once a twin is nucleated, it may also shrink via the emission of a shrinking partial on a plane adjacent to the twin boundary but on the twin side. De-twinning has been reported to be activated by the dynamic loading, as previously observed in nc NiFe alloys [73]. The critical stress to trigger a shrinking partial can be derived as [64]:

$$\tau_{shrink} = \frac{1}{\cos(\alpha+30^\circ)}\frac{\sqrt{6}(8+\nu)Ga}{48\pi(1-\nu)d} ln\frac{\sqrt{2}d}{a} \tag{10}$$

τ_{shrink} was calculated to be 1689 to 1000 MPa for NiCo with a grain size in the range of 27–52 nm. The larger the grain size, the smaller the critical stress needed to activate shrinking partial. The maximum shear flow stress of ~1000 MPa in nc NiCo alloy is high enough to activate de-twinning processes, especially at the late stage of dynamic deformation. Accordingly, we believe the suppression of DT and the activation of de-twinning induced the observed reduction of twin density in nc NiCo alloy.

For 70 nm nc Ni, 20~30% grains kept within the optimum grain size regime for DT over the whole strain range. Moreover, the final grain sizes of the two sets of nc Ni are both around 50 nm (Figs. 10b and 11b), just falling into the optimum grain size regime [70]. The τ_m for Ni was calculated to be 1,079 MPa according to Eq. (9). But if the γ_{utf} was considered, an extremely high τ_m can be expected (~3,000 MPa), which is much higher than the maximum shear flow stress achieved in both 27 and 70 nm Ni. Nevertheless, the stress concentration in SFs and GBs could easily overcome the energy barrier for twin nucleation posed by the high γ_{utf} [74]. The HSR can further intensify such stress concentrations. So, it is not unexpected that DT can be activated as a deformation mode in nc Ni, just as the cases at low temperatures [75] or under heavy deformations [76], where high stress level can also be achieved. Although de-twinning may also be activated, one can envision that a competition between DT and de-twinning, which could give rise to the slight increase in twin density.

6.2. Synergetic grain-size and strain-rate effects on microstructural evolution

In nc materials, high interfacial energy due to the large GB areas provides excessive driving forces for coarsening of the nano-grains. As a result, grain growth is highly prone to occur in nc materials when they are under mechanical loading and/or thermal exposure [77]. Although the initial grain sizes of these three materials all fall into the so-called real-nano regime, i.e., less than 100 nm, grain growth only occurred in the 27 nm Ni and NiCo alloy. In contrast, nano-grains in 70 nm Ni experienced a further refinement upon dynamic deformation, an unexpected phenomenon that has seldom been reported in other nc pure metals before.

Microstructural analysis reveals that grain coarsening in 27 nm Ni and NiCo alloy is achieved via grain coalescence (Fig. 8). The grain sizes in the 27 nm Ni and NiCo alloy fall just right into the so-called “lower nano” regime, where GB-mediated processes, including GB sliding, GB migration and grain rotations, play key roles in mediating plastic deformation [78]. The activation of GB-mediated processes is also corroborated by the texture evolution observed (Fig. 3). We believe that the observed grain growth in 27 nm Ni and NiCo alloy is the result of coalescence assisted by GB-mediated processes, commonly observed in other nc metals and alloys [79,80]. It was previously reported that nc NiCo alloys with high solute concentrations were stable against mechanical loading even when a high shear strain was imposed [21]. Alloying has also been found to improve the thermal stability of nc materials [81]. However, during dynamic deformation, a temperature rise from un-dissipated plastic work commonly occurs [61]. The temperature rise in the nc NiCo alloy during the present SHPB test was calculated to be 409 °C. This significant temperature rise could stimulate diffusive GB activities, thus facilitating grain coarsening. As nc materials can withstand simultaneously high flow stress and elevated temperature during dynamic deformation, it is not unexpected that grain coarsening can take place even in the nc NiCo alloy with high Co concentration.

In the 70 nm Ni, the temperature achieved during dynamic deformation is calculated to reach as high as 433 °C. Such high temperatures have been shown to promote significant grain coarsening easily in nc Ni with comparable grain size [82,83]. However, grain refinement, instead of coarsening, was observed in the 70 nm Ni during dynamic deformation. This observation is contrary to what would be normally expected and means that the nano-grains 70 nm Ni were first stabilized against coarsening and then experienced further refinement to a finer mean size of 56 nm. To our knowledge, this is a record low grain size induced by mechanical loading among all pure Ni ever reported. The stabilization of the nano-grains was enabled by the HSR via two mechanisms. First, because of the relatively large initial grain size and HSR, partial dislocation slip, including DT, plays an important role during the plastic deformation in 70 nm Ni (as discussed in Section 6.1). TEM observations of the deformed 70 nm Ni samples show that numerous SFs and DTs appear in remnant large nano-grains (Fig. S7a.b). It has been reported that such partial-dislocation-mediated activities can effectively relax GBs, lowering their energy [77,84]. Second, the nano-grains in the 70 nm Ni experienced a significant temperature rise within an extremely short time. Such rapid heating can also trigger intensive GB relaxation and, therefore, can induce a drop in GB energy [85]. As coarsening of the nano-grains is generally driven by the excess energy stored in the GBs, a reduction in GB energy means a reduction in driving force for coarsening, and thus enhanced stability [77]. The GB energy of the newly formed and smaller nano-grains can be effectively reduced by the grain-refining DT and GB-dissociation mechanisms [77]. Last, these just-refined nano-grains experienced rapid heating. All these factors work together to stabilize the GBs of the refined grains, changing the dominant plastic deformation from GB-mediated processes to the generation of extended partial dislocations, as evidenced by the presence of copious SFs and twins (Fig. S7c,d). Partial dislocation-mediated plasticity can, in turn, further relax the GBs, stabilizing the newly formed finer nano-grains. These processes explain why the 10–30 nm grains refined by dynamic loading survived after the severe shock deformation. This outcome is in sharp contrast to the substantial coarsening of the nano-grains ($d < 30$ nm) formed during electrodeposition in the 27 nm Ni and NiCo alloy. Such stability might be inferred from the grain refinement mechanism. It is also worth pointing out that the grain growth in the 27 nm Ni and Ni Co alloy induced by dynamic deformation was much less significant than those observed during conventional isothermally annealing [86]. This restrained grain coarsening may be also inferred from the GB relaxation resulting from the partial dislocation activities and rapid heating during dynamic deformation.

Based on the above discussion, it is conjectured that the grain-size dependent microstructural evolution mainly results from the predominant deformation mechanisms associated with the initial grain size of the samples. The activation of partial-slip activities, including DT, can induce GB relaxation to lower energy states and, therefore, stabilize the nano-grains. The enhanced stability observed is analogous to those seen in nc metals produced by dynamic plastic deformation [77,84,85]. We believe that, in both cases, HSR plays a key role by providing the high flow stresses required for emitting partial dislocations from GBs (as discussed in Section 6.1.2 and 6.1.3) and by stimulating rapid heating.

6.3. Grain size softening and hardening

The post-yielding decrease in flow stress can be clearly seen in the 27 nm Ni and NiCo alloy. In sharp contrast, the dynamic plastic flow in 70 nm Ni progressed in a much steadier manner with slight but positive strain hardening. Texture evolution could have caused these differences; however, despite the different initial textures in these three nc materials, they all evolve to a (110) texture. It is highly possible that the dynamic-induced variation of grain size played the most critical role in influencing the mechanical responses of nc Ni and NiCo alloys under shock loading. The flow softening present in the 27 nm Ni and NiCo alloy can be at-

tributed to the gradual grain coarsening and the adiabatic temperature rise when dynamic deformation proceeds [19]. Other reasons might be reductions in dislocation density and anomalous deprivation of DT (Figs. 9 and 10), which was previously reported to provide extra strain hardening in nanostructured materials during dynamic deformation [87]. For the 70 nm Ni, the initial stabilization of the large nano-grains facilitated subcequent grain refinement. The refined nano-grains formed during dynamic deformation strengthened the material, akin to a dynamic Hall-Petch effect. Moreover, in-situ grain refinement to nano-sizes is further stabilized by high-strain-rate deformation against coarsening, prohibiting grain-growth-induced strain softening. The increased dislocation density and DT also could have contributed to dynamic strain hardening (Fig. 11). As a result, a combination of high dynamic shear yield strength and large uniform dynamic plastic strain is achieved in the 70 nm Ni.

7. Conclusions

In summary, the findings achieved from the combined investigation of microstructure and texture evolution during dynamic deformation of two nc Ni materials and a nc NiCo alloy allow the following conclusions to be drawn:

Microstructural evolution in the three nc materials induced by dynamic deformation are strongly grain-size dependent. Evident grain growth was detected in the 27 nm nc Ni and nc NiCo alloy samples, while the 70 nm nc Ni sample experienced grain refinement. Such grain-size dependence mainly comes from the dependence of the predominant deformation mechanisms on the initial grain size of the samples. In the Ni and NiCo alloy with small average grain sizes of 27 nm, GB-mediated mechanisms prevailed at the early stages of dynamic deformation, promoting grain growth via rotation and coalescence. In contrast, the nc Ni with a large initial average grain size of 70 nm, a drop in GB energy due to the activation of partial dislocations and rapid heating stabilized the nano-grains and permitted further grain refinement.

Independent of the initial texture, all three materials evolved to a (110) texture after dynamic compression. Weakening of the initial (100) texture in the nc NiCo alloy was attributed to GB-mediated processes. Comparison of experimental and simulated deformation textures, together with the analysis based on GPFE curves, reveals that the formation of the (110) texture was induced by partial dislocation slip in the 27 nm NiCo, and by both partial and full dislocation slip in the two sets of nc Ni. In contrast to the conventional notion that nc materials prefer DT under HSR, DT contributed little to the observed texture evolution. The anomalous scarcity of DT can be rationalized based on the dynamic variation in grain size under shock loading and the grain size effect on DT in the nc regime.

The dynamic variation of grain size upon shock loading also substantially influenced the mechanical responses of the nc Ni and NiCo alloys. The dynamic Hall-Petch effect from the grain refinement in 70 nm Ni gave rise to a combination of high dynamic strength and uniform plastic strain, which is a superior dynamic mechanical property. In contrast, grain coarsening and concomitant adiabatic temperature rise caused continuous dynamic strain softening in the 27 nm Ni and NiCo alloy.

A D-CPFE model was developed to consider full and partial dislocation slip. This newly developed model can predict not only the trends in but also the rate of texture evolution under dynamic loading. The calculated deformation textures agree with the experimental deformed textures for all nc samples. The model revealed that partial dislocation slip induces faster texture evolution and stronger deformed textures at the same strain levels than full dislocation slip.

Declaration of Competing Interest

The authors declare that they have no known competing financial interests or personal relationships that could have appeared to influence the work reported in this paper.

Acknowledgments

The scientific and technical input and support from the Microscopy Australia node at the University of Sydney (Sydney Microscopy & Microanalysis) is appreciated. H. L. was supported by the China Scholarship Council. H. L. Z. was supported by the National Natural Science Foundation of China (grant No. 51871175). S. H. was supported by the National Natural Science Foundation of China (grant No. 51601067), the Science and Technology Development Program of Jilin Province (grant No. 20160520007JH) and the Program for JLU Science and Technology Innovative Research Team (JLUSTIRT, 2017TD-09). C. Z. was supported by the National Science Foundation CAREER Award (CMMI-1652662). I.J.B. acknowledges financial support from the National Science Foundation Designing Materials to Revolutionize and Engineer our Future (DMREF) program (NSF CMMI-1729887). X. Z. L. was supported by the Australian Research Council Discovery Project DP190102243. We acknowledge Dr. Xixun Shen and Dr. Jiangjiang Hu for their help in sample preparation. We express deep appreciation to Dr. Xun Sun for his contributions to the DFT calculations.

Supplementary materials

Supplementary material associated with this article can be found, in the online version, at doi:10.1016/j.actamat.2021.117088.

References

[1] M.A. Meyers, Dynamic Behavior of Materials, John Wiley & Sons, 1994.
[2] M.A. Meyers, B.A. Remington, B. Maddox, E.M. Bringa, Laser shocking of materials: toward the national ignition facility, JOM 62 (1) (2010) 24–30.
[3] B.E. Schuster, J.P. Ligda, Z.L. Pan, Q. Wei, Nanocrystalline refractory metals for extreme condition applications, JOM 63 (12) (2011) 27–31.
[4] S.A. Turnage, M. Rajagopalan, K.A. Darling, P. Garg, C. Kale, B.G. Bazehhour, I. Adlakha, B.C. Hornbuckle, C.L. Williams, P. Peralta, Anomalous mechanical behavior of nanocrystalline binary alloys under extreme conditions, Nat. Commun. 9 (1) (2018) 2699.
[5] I.A. Ovid'Ko, R.Z. Valiev, Y.T. Zhu, Review on superior strength and enhanced ductility of metallic nanomaterials, Prog. Mater. Sci. 94 (2018) 462–540.
[6] Q. Wei, D. Jia, K.T. Ramesh, E. Ma, Evolution and microstructure of shear bands in nanostructured Fe, Appl. Phys. Lett. 81 (7) (2002) 1240–1242.
[7] D. Jia, K.T. Ramesh, E. Ma, Effects of nanocrystalline and ultrafine grain sizes on constitutive behavior and shear bands in iron, Acta Mater. 51 (12) (2003) 3495–3509.
[8] Q. Wei, H.T. Zhang, B.E. Schuster, K.T. Ramesh, R.Z. Valiev, L.J. Kecskes, R.J. Dowding, L. Magness, K. Cho, Microstructure and mechanical properties of super-strong nanocrystalline tungsten processed by high-pressure torsion, Acta Mater. 54 (15) (2006) 4079–4089.
[9] C.H. Lu, B.A. Remington, B.R. Maddox, B. Kad, H.S. Park, M. Kawasaki, T.G. Langdon, M.A. Meyers, Laser compression of nanocrystalline tantalum, Acta Mater. 61 (20) (2013) 7767–7780.
[10] Q. Wei, Z.L. Pan, X.L. Wu, B.E. Schuster, L.J. Kecskes, R.Z. Valiev, Microstructure and mechanical properties at different length scales and strain rates of nanocrystalline tantalum produced by high-pressure torsion, Acta Mater. 59 (6) (2011) 2423–2436.
[11] Q. Wei, T. Jiao, K.T. Ramesh, E. Ma, Nano-structured vanadium: processing and mechanical properties under quasi-static and dynamic compression, Scr. Mater. 50 (3) (2004) 359–364.
[12] A. Novelli, C. Adembri, P. Livi, S. Vallani, T. Mazzei, A.R.D. Gaudio, Ultrahigh strength in nanocrystalline materials under shock loading, Science 309 (5742) (2005) 1838–1841.
[13] J.R. Trelewicz, C.A. Schuh, The Hall–Petch breakdown at high strain rates: optimizing nanocrystalline grain size for impact applications, Appl. Phys. Lett. 93 (17) (2008) 2681.
[14] Q. Wei, S. Cheng, K.T. Ramesh, E. Ma, Effect of nanocrystalline and ultrafine grain sizes on the strain rate sensitivity and activation volume: fcc versus bcc metals, Mater. Sci. Eng. A 381 (1-2) (2004) 71–79.
[15] J. Lian, C. Gu, Q. Jiang, Z. Jiang, Strain rate sensitivity of face-centered-cubic nanocrystalline materials based on dislocation deformation, J. Appl. Phys. 99 (7) (2006) 076103.

[16] Y.M. Wang, E.M. Bringa, J.M. McNaney, M. Victoria, A. Caro, A.M. Hodge, R. Smith, B. Torralva, B.A. Remington, C.A. Schuh, H. Jamarkani, M.A. Meyers, Deforming nanocrystalline nickel at ultrahigh strain rates, Appl. Phys. Lett. 88 (6) (2006) 061917.
[17] H. Swygenhoven, P.M. Van, A.G. Derlet, Fr?Seth, Stacking fault energies and slip in nanocrystalline metals, Nat. Mater. 3 (6) (2004) 399.
[18] X.L. Wu, Y. Qi, Y.T. Zhu, Partial-mediated slips in nanocrystalline Ni at high strain rate, Appl. Phys. Lett. 90 (22) (2007) 221911.
[19] C. Sheng, Z. Yonghao, G. Yazhou, L. Ying, W. Qiuming, W. Xun-Li, R. Yang, P.K. Liaw, C. Hahn, E.J. Lavernia, High plasticity and substantial deformation in nanocrystalline NiFe alloys under dynamic loading, Adv. Mater. 21 (48) (2010) 5001–5004.
[20] M. Yang, D. Yan, F. Yuan, P. Jiang, E. Ma, X. Wu, Dynamically reinforced heterogeneous grain structure prolongs ductility in a medium-entropy alloy with gigapascal yield strength, Proc. Natl. Acad. Sci. 115 (28) (2018) 7224–7229.
[21] R. Madhavan, S. Suwas, Micro-mechanisms of deformation texture evolution in nanocrystalline nickel-cobalt alloys, Acta Mater. 121 (2016) 46–58.
[22] Y. Ivanisenko, L. Kurmanaeva, J. Weissmueller, K. Yang, J. Markmann, H. Rösner, T. Scherer, H.-J. Fecht, Deformation mechanisms in nanocrystalline palladium at large strains, Acta Mater. 57 (11) (2009) 3391–3401.
[23] W. Skrotzki, A. Eschke, B. Jóni, T. Ungár, L.S. Tóth, Y. Ivanisenko, L. Kurmanaeva, New experimental insight into the mechanisms of nanoplasticity, Acta Mater. 61 (19) (2013) 7271–7284.
[24] U.F. Kocks, C.N. Tomé, H.-R. Wenk, Texture and Anisotropy: Preferred Orientations in Polycrystals and Their Effect on Materials Properties, Cambridge University Press, 1998.
[25] N.P. Gurao, S. Suwas, Texture evolution and operative mechanisms during large-strain deformation of nanocrystalline nickel, Philos. Mag. 91 (5) (2011) 798–817.
[26] R. Madhavan, S. Suwas, Deformation of nanograined Ni–60 Co alloy with low stacking fault energy, Philos. Mag. Lett. 94 (9) (2014) 548–555.
[27] C. Bin, L. Katie, R. Selva Vennila, Y. Jinyuan, K. Waruntorn, L. Jialin, Y. Shizhong, W. Hans-Rudolf, M. Ho-Kwang, W. Quentin, Texture of nanocrystalline nickel: probing the lower size limit of dislocation activity, Science 338 (6113) (2012) 1448–1451.
[28] C. Bin, L. Katie, L. Jialin, Y. Jinyuan, Y. Shizhong, M. Ho-Kwang, Detecting grain rotation at the nanoscale, Proc. Natl. Acad. Sci. U. S. A. 111 (9) (2014) 3350–3353.
[29] R. Madhavan, R.K. Ray, S. Suwas, New insights into the development of microstructure and deformation texture in nickel–60 wt.% cobalt alloy, Acta Mater. 78 (5) (2014) 222–235.
[30] R. Madhavan, R. Ray, S. Suwas, Texture transition in cold-rolled nickel–40 wt.% cobalt alloy, Acta Mater. 74 (2014) 151–164.
[31] G.C. Sneddon, P.W. Trimby, J.M. Cairney, Transmission Kikuchi diffraction in a scanning electron microscope: a review, Mater. Sci. Eng. R Rep. 110 (2016) 1–12.
[32] P.W. Trimby, Orientation mapping of nanostructured materials using transmission Kikuchi diffraction in the scanning electron microscope, Ultramicroscopy 120 (2012) 16–24.
[33] P.W. Trimby, Y. Cao, Z. Chen, S. Han, K.J. Hemker, J. Lian, X. Liao, P. Rottmann, S. Samudrala, J. Sun, J.T. Wang, J. Wheeler, J.M. Cairney, Characterizing deformed ultrafine-grained and nanocrystalline materials using transmission Kikuchi diffraction in a scanning electron microscope, Acta Mater. 62 (2014) 69–80.
[34] M.S. Pham, A. Creuziger, M. Iadicola, A.D. Rollett, Roles of texture and latent hardening on plastic anisotropy of face-centered-cubic materials during multi-axial loading, J. Mech. Phys. Solids 99 (2017) 50–69.
[35] S.Y. Li, E. Hoferlin, A. Van Bael, P. Van Houtte, C. Teodosiu, Finite element modeling of plastic anisotropy induced by texture and strain-path change, Int. J. Plast. 19 (5) (2003) 647–674.
[36] K.S. Cheong, E.P. Busso, Discrete dislocation density modelling of single phase FCC polycrystal aggregates, Acta Mater. 52 (19) (2004) 5665–5675.
[37] S. Chandra, M.K. Samal, V.M. Chavan, S. Raghunathan, Hierarchical multiscale modeling of plasticity in copper: from single crystals to polycrystalline aggregates, Int. J. Plast. 101 (2018) 188–212.
[38] X.Z. Liang, M.F. Dodge, J. Jiang, H.B. Dong, Using transmission Kikuchi diffraction in a scanning electron microscope to quantify geometrically necessary dislocation density at the nanoscale, Ultramicroscopy 197 (2019) 39–45.
[39] D.G. Brandon, The structure of high-angle grain boundaries, Acta Metall. 14 (11) (1966) 1479–1484.
[40] Y. Rui, I.J. Beyerlein, C. Zhou, Emergence of grain-size effects in nanocrystalline metals from statistical activation of discrete dislocation sources, Acta Mater. 90 (2015) 169–181.
[41] R. Yuan, I.J. Beyerlein, C. Zhou, Coupled crystal orientation-size effects on the strength of nano crystals, Sci. Rep. 6 (2016) 26254.
[42] R. Yuan, I.J. Beyerlein, C. Zhou, Statistical dislocation activation from grain boundaries and its role in the plastic anisotropy of nanotwinned copper, Acta Mater. 110 (2016) 8–18.
[43] T. Chen, R. Yuan, I.J. Beyerlein, C. Zhou, Predicting the size scaling in strength of nanolayered materials by a discrete slip crystal plasticity model, Int. J. Plast. 124 (2020) 247–260.
[44] E. Marin, P. Dawson, On modelling the elasto-viscoplastic response of metals using polycrystal plasticity, Comput. Methods Appl. Mech. Eng. 165 (1-4) (1998) 1–21.
[45] A. Foreman, The bowing of a dislocation segment, Philos. Mag. 15 (137) (1967) 1011–1021.
[46] E. Bitzek, P.M. Derlet, P.M. Anderson, H. Van Swygenhoven, The stress–strain response of nanocrystalline metals: a statistical analysis of atomistic simulations, Acta Mater. 56 (17) (2008) 4846–4857.
[47] A. Hunter, I. Beyerlein, Stacking fault emission from grain boundaries: material dependencies and grain size effects, Mater. Sci. Eng. A 600 (2014) 200–210.
[48] L. Vitos, Total-energy method based on the exact muffin-tin orbitals theory, Phys. Rev. B 64 (1) (2001) 014107.
[49] L. Vitos, The EMTO Method and Applications, in: Computational Quantum Mechanicals for Materials Engineers, Springer-Verlag, London, 2007.
[50] J.P. Perdew, K. Burke, M. Ernzerhof, Generalized gradient approximation made simple, Phys. Rev. Lett. 77 (1996) 3865–3868.
[51] S. Kibey, J.B. Liu, D.D. Johnson, H. Sehitoglu, Predicting twinning stress in fcc metals: linking twin-energy pathways to twin nucleation, Acta Mater. 55 (20) (2007) 6843–6851.
[52] H. Alimadadi, A.B. Fanta, T. Kasama, M.A.J. Somers, K. Pantleon, Texture and microstructure evolution in nickel electrodeposited from an additive-free Watts electrolyte, Surface Coatings Technol. 299 (2016) 1–6.
[53] K. Schüler, B. Philippi, M. Weinmann, V.M. Marx, H. Vehoff, Effects of processing on texture, internal stresses and mechanical properties during the pulsed electrodeposition of nanocrystalline and ultrafine-grained nickel, Acta Mater. 61 (11) (2013) 3945–3955.
[54] X.Y. Zhang, X.L. Wu, Q. Liu, R.L. Zuo, A.W. Zhu, P. Jiang, Q.M. Wei, Phase transformation accommodated plasticity in nanocrystalline nickel, Appl. Phys. Lett. 93 (3) (2008) 031901.
[55] M.A. Meyers, Y.B. Xu, Q. Xue, M.T. Pérez-Prado, T.R. McNelley, Microstructural evolution in adiabatic shear localization in stainless steel, Acta Mater. 51 (5) (2003) 1307–1325.
[56] R. Sonkusare, R. Jain, K. Biswas, V. Parameswaran, N.P. Gurao, High strain rate compression behaviour of single phase CoCuFeMnNi high entropy alloy, J. Alloys Compd. 823 (2020) 153763.
[57] H.J. Gao, Y.G. Huang, Geometrically necessary dislocation and size-dependent plasticity, Scr. Mater. 48 (2) (2003) 113–118.
[58] Y. Cao, S. Ni, X. Liao, M. Song, Y. Zhu, Structural evolutions of metallic materials processed by severe plastic deformation, Mater. Sci. Eng. R Rep. 133 (2018) 1–59.
[59] Y.B. Wang, X.Z. Liao, Y.H. Zhao, E.J. Lavernia, S.P. Ringer, Z. Horita, T.G. Langdon, Y.T. Zhu, The role of stacking faults and twin boundaries in grain refinement of a Cu–Zn alloy processed by high-pressure torsion, Mater. Sci. Eng. A 527 (18-19) (2010) 4959–4966.
[60] A. Cao, Y. Wei, Atomistic simulations of crack nucleation and intergranular fracture in bulk nanocrystalline nickel, Phys. Rev. B 76 (2) (2007) 4113.
[61] M. Yan, F. Yuan, M. Yang, J. Ping, E. Ma, X. Wu, Dynamic shear deformation of a CrCoNi medium-entropy alloy with heterogeneous grain structures, Acta Mater. 148 (2018) S1359645418301174.
[62] W.F. Hosford, Mechanical Behavior of Materials, Cambridge University Press, 2010.
[63] K. Tao, D.W. Brown, S.C. Vogel, H. Choo, Texture evolution during strain-induced martensitic phase transformation in 304L stainless steel at a cryogenic temperature, Metall. Mater. Trans. A 37 (12) (2006) 3469–3475.
[64] Y.T. Zhu, X.Z. Liao, X.L. Wu, Deformation twinning in nanocrystalline materials, Prog. Mater. Sci. 57 (1) (2012) 1–62.
[65] Y.T. Zhu, X.Z. Liao, S.G. Srinivasan, E.J. Lavernia, Nucleation of deformation twins in nanocrystalline face-centered-cubic metals processed by severe plastic deformation, J. Appl. Phys. 98 (3) (2005) 034319.
[66] G.T.G. Iii, High-strain-rate deformation: mechanical behavior and deformation substructures induced, Annu. Rev. Mater. Res. 42 (1) (2012) 285–303.
[67] S. Suwas, R.K. Ray, Crystallographic Texture of Materials, Springer, 2014.
[68] R.J. Asaro, S. Suresh, Mechanistic models for the activation volume and rate sensitivity in metals with nanocrystalline grains and nano-scale twins, Acta Mater. 53 (12) (2005) 3369–3382.
[69] A.G. Frøseth, P.M. Derlet, H. Van Swygenhoven, Twinning in nanocrystalline FCC metals, Adv. Eng. Mater. 7 (1-2) (2005) 16–20.
[70] X.L. Wu, Y.T. Zhu, Inverse grain-size effect on twinning in nanocrystalline Ni, Phys. Rev. Lett. 101 (2) (2008) 025503.
[71] Y.T. Zhu, X.Z. Liao, X.L. Wu, J. Narayan, Grain size effect on deformation twinning and detwinning, J. Mater. Sci. 48 (13) (2013) 4467–4475.
[72] Y. Zhu, X. Liao, S. Srinivasan, Y. Zhao, M. Baskes, F. Zhou, E. Lavernia, Nucleation and growth of deformation twins in nanocrystalline aluminum, Appl. Phys. Lett. 85 (21) (2004) 5049–5051.
[73] S. Cheng, Y. Zhao, Y. Wang, Y. Li, X.-L. Wang, P.K. Liaw, E.J. Lavernia, Structure modulation driven by cyclic deformation in nanocrystalline NiFe, Phys. Rev. Lett. 104 (25) (2020) 255501.
[74] X.-L. Wu, Y.T. Zhu, E. Ma, Predictions for partial-dislocation-mediated processes in nanocrystalline Ni by generalized planar fault energy curves: an experimental evaluation, Appl. Phys. Lett. 88 (12) (2006) 121905.
[75] X. Wu, Y.T. Zhu, M.W. Chen, E. Ma, Twinning and stacking fault formation during tensile deformation of nanocrystalline Ni, Scr. Mater. 54 (9) (2006) 1685–1690.
[76] S. Han, L. Zhao, G.Y. Wang, J.S. Lian, Revealing the intrinsic dislocation storage capability in nanocrystalline nickel, Mater. Lett. 127 (2014) 20–23.
[77] X. Zhou, X.Y. Li, K. Lu, Enhanced thermal stability of nanograined metals below a critical grain size, Science 360 (6388) (2018) 526–530.
[78] E. Ma, Materials science. watching the nanograins roll, Science 305 (5684) (2004) 623.

[79] X.Z. Liao, A.R. Kilmametov, R.Z. Valiev, H. Gao, X. Li, A.K. Mukherjee, J.F. Bingert, Y.T. Zhu, High-pressure torsion-induced grain growth in electrodeposited nanocrystalline Ni, Appl. Phys. Lett. 88 (2) (2006) 021909.
[80] Y.B. Wang, J.C. Ho, Y. Cao, X.Z. Liao, H.Q. Li, Y.H. Zhao, E.J. Lavernia, S.P. Ringer, Y.T. Zhu, Dislocation density evolution during high pressure torsion of a nanocrystalline Ni–Fe alloy, Appl. Phys. Lett. 94 (9) (2009) 191–199.
[81] T. Chookajorn, H.A. Murdoch, C.A. Schuh, Design of stable nanocrystalline alloys, Science 337 (6097) (2012) 951–954.
[82] H.W. Zhang, X. Huang, R. Pippan, N. Hansen, Thermal behavior of Ni (99.967% and 99.5% purity) deformed to an ultra-high strain by high pressure torsion, Acta Mater. 58 (5) (2010) 1698–1707.
[83] X.C. Liu, H.W. Zhang, K. Lu, Strain-induced ultrahard and ultrastable nanolaminated structure in nickel, Science 342 (6156) (2013) 337–340.
[84] X. Zhou, X. Li, K. Lu, Size dependence of grain boundary migration in metals under mechanical loading, Phys. Rev. Lett. 122 (12) (2019) 126101.
[85] X.Y. Li, X. Zhou, K. Lu, Rapid heating induced ultrahigh stability of nanograined copper, Sci. Adv. 6 (17) (2020) 6.
[86] G.D. Hibbard, K.T. Aust, U. Erb, Thermal stability of electrodeposited nanocrystalline Ni–Co alloys, Mater. Sci. Eng. A 433 (1) (2006) 195–202.
[87] Y.M. Wang, J.Y. Huang, T. Jiao, Y.T. Zhu, A.V. Hamza, Abnormal strain hardening in nanostructured titanium at high strain rates and large strains, J. Mater. Sci. 42 (5) (2007) 1751–1756.